JOURNAL OF SYNCHROTRON RADIATION
ISSN 1600-5775

Non-negative matrix factorization for the near real-time interpretation of absorption effects in elemental distribution images acquired by X-ray fluorescence imaging

Matthias Alfeld,[a]* Mirwaes Wahabzada,[b,c] Christian Bauckhage,[c] Kristian Kersting,[c,d] Gerd Wellenreuther,[e] Pere Barriobero-Vila,[f] Guillermo Requena,[g] Ulrike Boesenberg[a] and Gerald Falkenberg[a]

[a]Deutsches Elektronen-Synchrotron DESY, Notkestraße 85, Hamburg 22607, Germany, [b]INRES – Pflanzenkrankheiten und Pflanzenschutz, Universität Bonn, Meckenheimer Allee 166a, Bonn 53115, Germany, [c]Fraunhofer IAIS, Schloss Birlinghoven, Sankt Augustin 53757, Germany, [d]Computer Science Department, TU Dortmund University, Joseph-von-Fraunhofer-Straße 23, Dortmund 44227, Germany, [e]European XFEL GmbH, Albert-Einstein-Ring 19, Hamburg 22761, Germany, [f]Institute of Materials Science and Technology, Vienna University of Technology, Karlsplatz 13/E308, Vienna 1040, Austria, and [g]Institute of Materials Research, German Aerospace Center, Linder Höhe, Köln 51147, Germany. *Correspondence e-mail: matthias.alfeld@upmc.fr

Received 2 September 2015
Accepted 7 December 2015

Edited by S. M. Heald, Argonne National Laboratory, USA

Keywords: micro-XRF; data analysis; non-negative matrix factorization; NMF; Ti alloys.

Supporting information: this article has supporting information at journals.iucr.org/s

Elemental distribution images acquired by imaging X-ray fluorescence analysis can contain high degrees of redundancy and weakly discernible correlations. In this article near real-time non-negative matrix factorization (NMF) is described for the analysis of a number of data sets acquired from samples of a bi-modal $\alpha+\beta$ Ti-6Al-6V-2Sn alloy. NMF was used for the first time to reveal absorption artefacts in the elemental distribution images of the samples, where two phases of the alloy, namely α and β, were in superposition. The findings and interpretation of the NMF results were confirmed by Monte Carlo simulation of the layered alloy system. Furthermore, it is shown how the simultaneous factorization of several stacks of elemental distribution images provides uniform basis vectors and consequently simplifies the interpretation of the representation.

1. Introduction

X-ray fluorescence spectroscopy (XRF) imaging is a suitable tool for the investigation of samples at different length scales. The most advanced instruments for this technique are at beamlines employing synchrotron radiation, such as the X-ray Micro/Nano-Probe beamline P06 at the Deutsches Elektronen-Synchrotron (DESY) in Hamburg, Germany (Schroer *et al.*, 2010). The beamline was designed for the investigation of samples from a wide range of scientific fields in a flexible sample environment. The investigated samples cover the fields of biology (Mishra *et al.*, 2013), materials science (Boesenberg *et al.*, 2015) and cultural heritage (Monico *et al.*, 2015).

A large fraction of available synchrotron time is dedicated to external users at these experimental end-stations. Commonly, these time slots (beam times) are rather short and consist of only a few days. In order to make efficient use of time provided at a beamline, at least the preliminary interpretation of data during an experiment is necessary. This provides a twofold challenge, as the users might be unfamiliar with the exact experimental conditions and data analysis, while the scientific staff at the beamline might be unfamiliar with the samples.

The fundamental processes of XRF analysis are well understood and the calculation of raw intensities of (groups

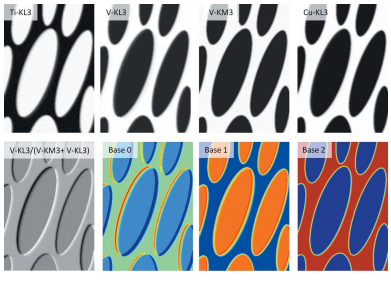

of) individual fluorescence lines from experimental data has been realised in a range of software packages (Ryan & Jamieson, 1993; Vekemans *et al.*, 1994; Vogt, 2003; Solé *et al.*, 2007; Alfeld & Janssens, 2015). Advanced software packages allow for a real-time or near real-time processing of the acquired data so that elemental distribution images are available during the beam time.

In multiphase samples containing concentration variations of the same elements between phases, compositional changes may not be immediately revealed. Then, the interpretation of elemental distribution images is not always straightforward, especially if the scientist is not familiar with the scientific background of the sample. Matrix factorization supports the interpretation of stacks of elemental distribution images by removing redundancies and highlighting correlations. Furthermore, it supports an interpretation of the experimental results unbiased by the user's expectations.

In matrix factorization, the data matrix V with its spectral dimension d (here the individual elemental distribution images) and the number of pixels n is represented by the product of a number of k basis vectors W and coefficients H (Fig. 1). From the original three-dimensional data (two lateral and one spectral dimension) a two-dimensional data matrix V is calculated by reshaping the array. The base vectors W represent the loading of individual elemental lines on the bases, while the coefficients H show the contribution of each base to an individual pixel. The coefficients H for each base k can be reshaped into two-dimensional images with the same lateral coordinate system as the original elemental distribution images. For clarification, all elemental distribution images in this paper are in grey-scale, while all factorization results are in colour-scale.

It is obvious that many combinations of basis vectors W and coefficients H describe the data matrix V, and the rules used to determine W and H have a strong influence on the representation obtained. Also, to support a fast interpretation of data during an experiment, an easy and clear representation prevails upon a complete one. To facilitate this at beamline P06, a joint project of the Fraunhofer IAIS and DESY was started to implement fast matrix factorization algorithms for near real-time analysis of acquired data during beam time.

Principal component analysis (PCA) is probably the most often used matrix factorization algorithm. It allows straightforward calculation of basis vectors and coefficients (usually termed loads and scores, respectively). Using this algorithm, all basis vectors are orthogonal and all coefficients orthonormal. Due to these constrains the basis vectors and coefficients may contain negative values. However, all signals acquired during XRF imaging experiments are positive, and negative values in the representation are unphysical and difficult to be intuitively interpreted. For this reason, the interpretation of PCA data requires significant experience. The limitations of PCA can be partially resolved by clustering the data, leading to easily interpretable basis vectors but coefficients of binary nature (Vekemans *et al.*, 1997).

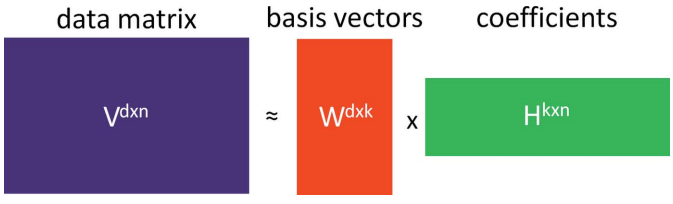

Figure 1
Principle of matrix factorization: the data matrix V with the spectral dimension d and the number of pixels n is represented by a set of k basis vectors W and coefficients H.

In search of an algorithm that allows a fast, robust matrix factorization approach that yields easily interpretable representations, we came to non-negative matrix factorization (NMF) (Lee & Seung, 1999). Using this algorithm, W and H are initiated with random values and updated in an iterative process, leading to a representation that preserves the non-negative nature of XRF data sets and resolves many correlations. A good criterion for convergence to be used as a response function is the Frobenius norm[1] and variations of it. However, for the analysis of spectromicroscopy data other measures have also been recently proposed (Mak *et al.*, 2014).

Matrix factorization with non-negative constrains has long been used in spectroscopic imaging (Kotula *et al.*, 2003), but has found only limited use in the interpretation of XRF imaging data until now. Osan *et al.* used positive matrix factorization of the *EPA PMF 3.0* software package in a study on the sorption capacity of claystone for several radionuclides, to identify the most strongly absorbing mineral phases (Osán *et al.*, 2014; Kéri *et al.*, 2016). Lahlil *et al.* used the NMF routines implemented in the *PyMCA* software package to identify components present in micro-XRF maps of lead antimonate-based opacifiers in glass samples from several epochs (Lahlil *et al.*, 2011). Santos *et al.* used the same routines to identify in a full spectral XRF data set of an enamel plaque the correlation of several elements of an anachronistic pigment and so revealed the object to be a 19th century forgery (Santos *et al.*, 2016). Our group used the NMF function of the Python Matrix Factorization module (pymf) (https://code.google.com/p/pymf/) for the interpretation of elemental distribution images of several thousand square centimetres of a Rembrandt painting to discriminate between chemical components with identical qualitative but different quantitative chemical composition (Alfeld *et al.*, 2014).

Based on this experience we found NMF suitable for use at beamline P06 during and after XRF imaging experiments. A suitable GUI for online analysis was developed and is now integrated in the data evaluation procedures at beamline P06. The GUI, which was used to obtain the results presented in this paper, will soon be published as open source after a period of internal testing (https://sourceforge.net/projects/p06pymfgui/). In this publication we illustrate the value of NMF analysis in supporting the fast and intuitive interpretation of XRF imaging data associated with the study of phase transformation kinetics during continuous heating of a bimodal $\alpha+\beta$ Ti-6Al-6V-2Sn alloy (Barriobero-Vila *et al.*, 2015*a*).

[1] Frobenius norm F: $F = \left(\sum_{n=1}^{n} \sum_{d=1}^{d} |V - WH|^2 \right)^{1/2}$.

$\alpha+\beta$ Titanium alloys present special interest for the aerospace and land transportation industry since they feature high specific strength, fatigue resistance and excellent corrosion resistance (Banerjee & Williams, 2013). The mechanical properties of these alloys are essentially determined by their microstructure, which is controlled by thermal and thermo-mechanical treatments during manufacturing. Therefore, advances in functional alloy design and cost reduction of components are strongly dependent on the correct understanding of the phase transformation kinetics (Barriobero-Vila *et al.*, 2015*a*,*b*). The diffusion mechanisms controlling these processes have been generally explained on the basis of theoretical equilibrium concentrations of alloying elements between phases. Recently, the role of element partitioning on the α–β phase transformation kinetics of a bi-modal $\alpha+\beta$ Ti-6Al-6V-2Sn was studied experimentally by micro-XRF, revealing variations in the transformation sequence with the heating rate (Barriobero-Vila *et al.*, 2015*a*). In addition to the elemental distribution images acquired by micro-XRF at beamline P06, *in situ* high-energy synchrotron X-ray diffraction (HEXRD) was carried out at the ID15B beamline of the European Synchrotron Radiation Facility (ESRF), Grenoble, France. Moreover, scanning electron microscopy with energy-dispersive X-ray spectroscopy (SEM-EDX) as well as conventional metallographic analysis were applied. In the SEM images it was clearly visible that next to the large volumes of the primary α phase a secondary α phase also exists, which is enclosed in small volumes inside the β phase. These volumes of the secondary α are smaller than the beam used for XRF imaging at P06 and are thus not resolved and only detected as a minor concentration variation, which was found to have no influence on data evaluation in the further paper. For high-resolution SEM images the reader is referred to the original publication (Barriobero-Vila *et al.*, 2015*a*).

The experiments at P06 aimed at the acquisition of elemental distribution images that featured, next to a high lateral resolution, also statistics and contrast superior to SEM-EDX images to study the element partitioning especially for stabilizers of the β phase, *i.e.* V, Fe and Cu. The near real-time NMF analysis provided crucial information that prevented a potential misinterpretation of the acquired data.

In the following, the samples and the technical details concerning the acquisition of elemental distribution images by XRF will be described. It will be shown how NMF allowed to highlight artefacts that hindered a clear understanding of the images and how Monte Carlo simulation confirmed our interpretation of them as absorption effects. Finally, alternatives to the NMF approach used will be discussed.

2. Experimental

2.1. Sample preparation

Eight samples of the Ti-6Al-6V-2Sn alloy were investigated by micro-XRF at beamline P06. They were subjected to different thermal treatments that comprise an initial continuous heating using 5 and 100°C min^{-1} followed by helium quenching of samples at different temperatures. To enhance readability only three of the measured samples will be discussed in this paper (see Table 1). Samples of ∼10 µm thickness and 4 mm × 4 mm area were obtained for the XRF imaging experiments by grinding and polishing of the thermal treated samples in a Multiprep machine. Details on sample preparation can be found in the original study (Barriobero-Vila *et al.*, 2015*a*). The concentration of minor components in the bulk material was given by the manufacturer as Al 6 wt%, V 6 wt%, Sn 2 wt%, Cu 0.75 wt% and Fe 0.35–1 wt%.

Table 1
Samples investigated.

Sample	Heating rate (°C min^{-1})	Quenching temperature (°C)
A	5	940
B	5	530
C	100	590

2.2. XRF imaging at beamline P06

The elemental distribution images discussed in this publication were acquired at the Microprobe end-station of beamline P06. The third harmonic from a 2 m spectroscopy undulator was selected by means of a cryogenically cooled Si(111) double-crystal monochromator, yielding a primary beam of 11.5 keV. A Kirkpatrick–Baez mirror system (KB) was used to focus the beam down to approximately 0.5 µm × 0.5 µm at the site of the sample, on which it impinged near normal angle. The fluorescence radiation emitted by the sample was recorded by means of a Vortex EM detector (50 mm^2 active area), on which a conical collimator was mounted to reduce the contribution from primary radiation scattered by the air. The intensity of the primary beam was monitored by means of an ionization chamber positioned before the KB system, and a passivated implanted planar silicon (PIPS) diode positioned behind the sample. The latter allowed for the acquisition of images featuring the intensity of the transmitted radiation.

The sample was positioned in the focus of the beam and rotated until the detector featured an out-going count rate of 20 kcounts s^{-1}. This procedure prevented the overexposure of the detector during the measurement and assured a comparable, albeit not identical, detection geometry between different samples. Consequently, the detection angle varied around 5° with an air path length of approximately 2.5 cm, which is considered acceptable for non-quantitative results. Areas of 10 µm × 10 µm were scanned with 0.5 µm step size and a dwell time of 0.2 s per pixel, consequently taking roughly 135 min per sample. Under the chosen experimental conditions Sn-*L* lines were only weakly excited and strongly absorbed in the air path between sample and detector, so that their distribution could not be imaged.

Elemental distribution images were obtained in a few minutes by linear least-squares fitting in *PyMCA* (Solé *et al.*, 2007) and corrected for beam intensity and dwell time varia-

tions in in-house-written software. Gamma correction was used on all images shown in order to enhance their readability.

3. Results and discussion

3.1. Elemental distribution images

In Fig. 2 elemental distribution images of the samples *A* to *C* are shown. In the red and yellow binary images each pixel is attributed belonging predominantly to the primary α phase (yellow) and β phase (red) based on a comparison of the intensity of the Cu-K_α signal with an empirical threshold. The noisy appearance of the Ti-*K* and transmission intensity images of the detail are due to incomplete correction for variations of the primary beam's intensity.

Sample *A*, which was heated at 5°C min^{-1} up to 940°C, presents a matrix of β phase rich in V with only a small ∼10 vol% of primary α phase (relatively richer in Ti) (Barriobero-Vila *et al.*, 2015*a*). In the V distribution image it can be seen that the V signal decreases with proximity to the α grains. At the interface the signal is decreased by 10% compared with that of the bulk β phase. The distribution of the weaker absorbing α phase in the depth of the sample is discernible in the transmission image. This confirms that the depletion of V in the α/β interphase is not an artefact due to underlying phases but a concentration gradient. The other stabilizers of the β phase, namely Fe, Cu and Ni (the latter was found with a lower concentration level), are also mainly present in the β phase. Differently to V, they do not show clear variations in the interphase. Furthermore, the statistics of the V-K_β image only give a vague impression of the enrichment due to the noisy image obtained from the lesser intense fluorescence line.

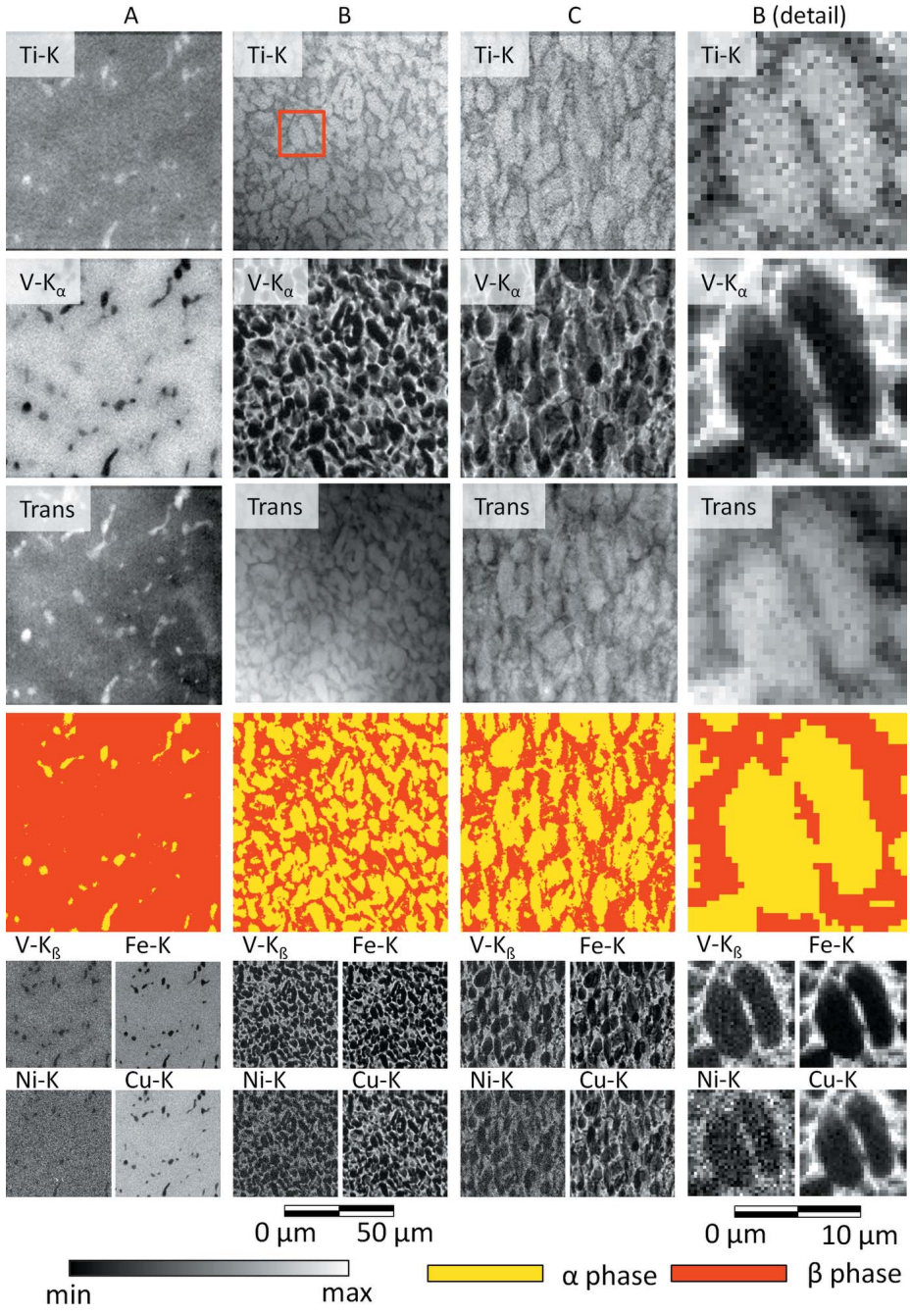

Figure 2
Elemental distribution images of 10 µm × 10 µm with a step size of 0.5 µm and a dwell time of 0.2 s of samples *A*, *B* and *C* (left to right). Two primary α grains of sample *B* are shown in the rightmost column, as indicated in the Ti-*K* distribution image. 'Trans' indicates the intensity of the radiation transmitting through the sample. To guide the eye, the pixels predominantly belonging to the α phase are coloured yellow and those predominantly belonging to the β phase are red, in the binary images. The scale bars refer to the large overview images; the images in the bottom row are half of this.

Samples *B* and *C* were heated up to moderate temperatures (see Table 1) and present less easily interpretable images. Here, α amounts to ∼88 and 85 vol% for 5 and 100°C min^{-1}, respectively (Barriobero-Vila *et al.*, 2015*a*). Also, the primary α and β phases are clearly discernible in the Ti-*K* and transmission signal images. However, as primary α and β phases are much closer to one another a clear distinction on a per-pixel base is more difficult. The difference in signal intensity in the lower left corner of sample *B* is due to variations of sample thickness.

After seeing concentration variations in the β phase boundaries of sample *A*, it is tempting to search for similar

effects in the images of the samples *B* and *C*. Indeed, a close inspection of the V-K_α distribution images of these samples reveals also a gradient of the recorded signal's intensity in the boundaries between primary α and β phases. This is especially clear in the upper part of the two representative primary α phase grains, shown in the rightmost column of Fig. 2. Similar gradients are weakly discernible in the element distribution of the other stabilizer elements of β, *i.e.* Fe, Cu and Ni [shown in Digital Supporting Information (DSI) 0.1 of the supporting information].

In backscatter electron images and classical metallographic light microscopic images, which practically probe only the surface of the sample, the border between α and β phases can be easily defined by setting a global threshold in the intensity of the displayed signal. This approach is less accurate for elemental distribution images of the elements obtained by micro-XRF since the recorded fluorescence radiation can penetrate through several micrometres of the sample. Therefore, sub-surface features can contribute to the acquired elemental distribution image. However, quantification of this effect is difficult. To gain additional insight into the elemental distribution images, NMF was used.

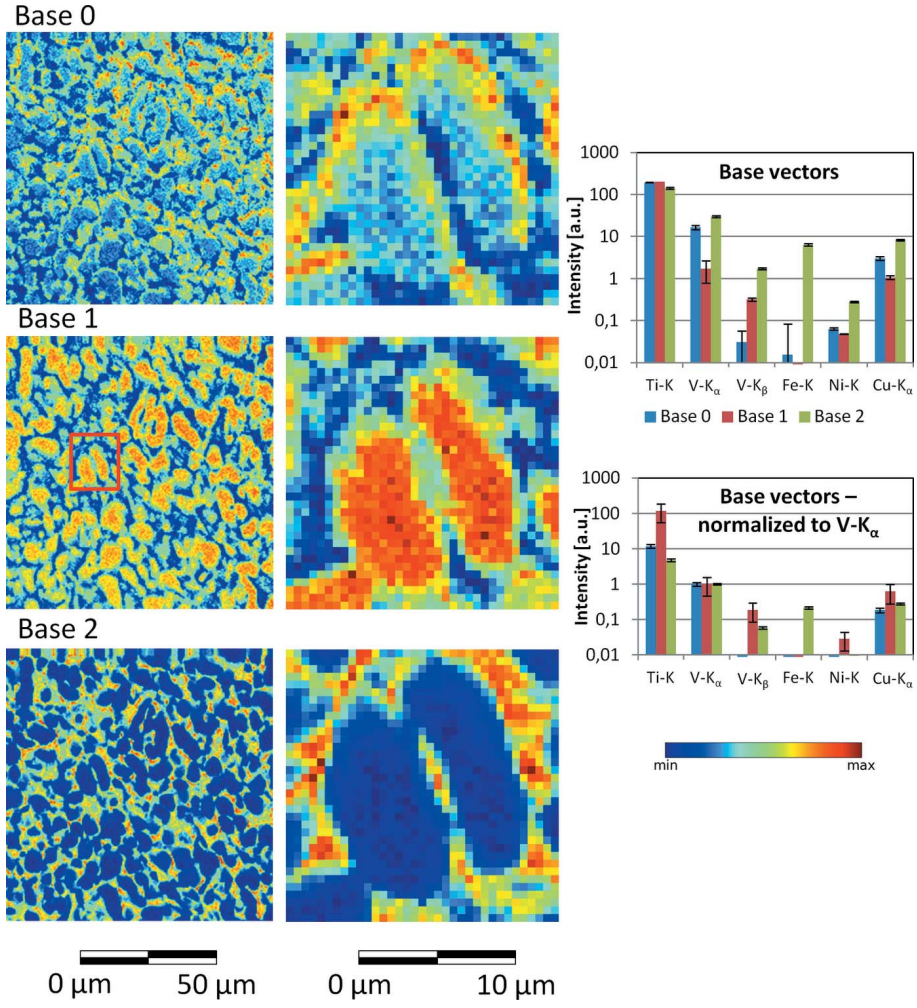

Figure 3
Typical coefficient images obtained by NMF from the data set of sample *B* only. The base vectors feature average loads and their sample standard deviation, calculated from the 71 successful NMF attempts. The area of the detail is indicated in the coefficient image of Base 1.

3.2. Non-negative matrix factorization

For the data set of sample *B* the elemental distribution images obtained by fitting with *PyMCA* were analyzed with NMF. As data matrix the elemental distribution images shown in Fig. 2 were selected, omitting those unrelated to the sample, such as that of Ar. Prior to factorization each elemental distribution image was normalized to the square root of its mean value (Vekemans *et al.*, 1997). This form of normalization was found best for the factorization of elemental distribution images, as un-normalized data are dominated by the strongest element, in this case Ti. In the case of normalization to the mean value of elemental distribution images the random noise in distribution images of weakly contributing elements was found to be given too much weight. After factorization the base vectors were rescaled to normal values.[2]

The number of bases k was empirically determined. Given the presence of two phases with different elemental composition in the Ti-6Al-6V-2Sn alloy, the number of bases k had to be larger than two. Three bases were used in the factorization, as with more bases the NMF did not properly converge, yielding several noisy coefficient images which represented together the α phase (shown in DSI 1.1 of the supporting information). In other studies we used the number of significant PCA bases to estimate the number of bases k in a NMF factorization.

The data set was factorized with 3000 iterations and aborted when the improvement of the Frobenius norm in an iteration of the NMF was less than 1 p.p.m.. The factorization was repeated 99 times with different seeds for the random initial values of H and W. Seventy-one results comparable with those presented in Fig. 3 were returned. The presence of a third component was not recognized 20 times, and the β phase was represented by one base, while the α phase was represented by two bases, yielding noisy images, clearly indicating that the factorization had failed (shown in DSI 1.2 of the supporting

[2] Not normalized coefficients were obtained by multiplication with the inverse of the normalization matrix C: $C^{d\times d}\times V^{d\times n} \approx C^{d\times d}\times W^{d\times k}\times H^{k\times n}$; $(C^{d\times d})^{-1}\times C^{d\times d}\times W^{d\times k} = W^{d\times k}$.

information). Three phases were found eight times, but Base 0 and Base 2 were not clearly resolved. This is basically worse than a 'failed' factorization as the failure is not obvious to the user (shown in DSI 1.3 of the supporting information). The successful factorizations took on average 17.7 s on a normal office PC[3] and converged after 1550 iterations on average. Given the rather swift processing of the data set the parameters of the NMF could be empirically improved and results were provided in a short time compared with data acquisition (more than 2 h).

From the 71 'good' factorizations the mean basis vector values for each element were calculated, as well as their sample standard deviation. For most elements the sample standard deviation is less than 12%; however, especially weak contributions to one base can have a sample standard deviation of several hundred percent.

Of the 'good' factorization shown in Fig. 3, Base 1 and Base 2 represent primary α and β phases, respectively. Base 1 features a strong contribution from Ti and weaker contributions from all other elements and is similar to the composition of the primary α phase. Base 2 features a higher contribution of the stabilizing minor elements of the β phase. The coefficient images of both bases are in good agreement with the distribution of the two phases concluded from the elemental distribution images. Base 0 is more difficult to interpret. In its elemental composition it resembles more the β than the primary α phase, but more striking is its distribution. It is of moderate intensity in areas dominated by the primary α phase and presents high intensity in some of its boundaries, showing a structured anisotropic distribution. In the detail shown the high-intensity boundaries are mainly upwards and to the right. In the rest of the data set no general preference for a single direction can be observed. The contribution of Base 0 is very low in areas dominated by the β phase and weak in that dominated by the α phase.

The rise of the V-K_α signal inside the primary α phase was assumed to be an artefact resulting from absorption effects and not a true enrichment of V and other stabilizers of the β phase, as diffusive processes are not expected to favour one lateral direction during thermal treatment. In Base 0 the effect from the thickness variation of the sample is also visible, showing a stronger contribution in the upper right corner than in the lower left.

Also the elemental distribution images of the samples *A* and *C* were investigated with NMF. While in the literature matrix factorization is, with few exceptions (De Juan *et al.*, 2004), limited to single scans, we combined the images of all three samples into one data matrix and processed it with the same settings (number of bases, maximum number of iterations, convergence criterion) as the images of sample *B* in less than 1 min to determine bases and coefficients.

The results, shown in Fig. 4, are in good agreement for sample *B* with the individual processing, yielding similar basis vectors and coefficient images (Fig. 3). The difference between the basis vectors normalized to V obtained by both approaches is in general less than one standard deviation. This is, however, not true for the Ni-*K* signal of Base 0 and the V-K_α signal of Base 2, which differ by 4.0 and 1.5, respectively, standard deviations. In the NMF results of sample *C* a representation similar to sample *B* was found. Base 1 represents the primary α phase, Base 2 the β phase matrix and Base 0 features the anisotropic distribution located at the boundaries of the primary α phase.

The results of sample *A* are different. Base 1 still represents the primary α phase, while the β phase matrix is represented by Bases 0 and 2, with Base 0 having a stronger contribution. It is not surprising that Base 0 with its lesser relative V contribution is stronger, as the same absolute mass of V is now distributed over a larger volume of β phase and so its concentration is reduced. The concentration variation of V at the boundaries between β and primary α phase is represented by the addition of Base 1 to Base 2 in the absence of Base 0. However, it is crucial that no anisotropic effects similar to the samples *B* and *C* were observed for sample *A*.

The factorization of all samples in parallel simplifies the interpretation of NMF data considerably, as only one set of basis vectors needs to be interpreted, but it requires comparable measurement conditions and similar samples.

If processed individually, the data sets of the samples *A* and *C* featured a slightly improved contrast and similar sample standard deviation of the elemental contributions to the basis vectors. The parameters used for NMF in this section, *i.e.* *k*, elemental maps used, normalization method, maximum number of iterations, and threshold for interrupting the factorization, were adjusted to obtain easily readable results. However, the presence of a third base, next to those for the two phases, was immediately apparent, as was its anisotropic distribution around the grains of the primary α phase.

3.3. Monte Carlo simulation

The exact meaning of the anisotropic distribution of Base 0 around the primary α grains remained puzzling after NMF analysis. It was assumed to be caused by superposition of primary α and β phases and the resulting absorption effects in some areas, but the magnitude of this effect for different elements was difficult to estimate and required further analysis.

As discussed in the *Introduction*, the fundamental physical interactions giving rise to XRF signals are well understood. An approximation of the intensity of fluorescence lines based on analytical calculations using the fundamental parameter approach is straightforward, but to take secondary excitation in layered structures into account is not. A solution to this is Monte Carlo simulation (MC), in which the interaction between primary photons and the sample is simulated as a number of random events with probabilities based on fundamental parameters.

The system simulated is shown at the bottom of Fig. 5. The sample has a uniform thickness of 10 µm. At the very left the sample is pure β phase, featuring strong signals of V, Fe and Cu. Then a layer of α phase is superimposed and grows in

[3] Intel QuadCore CPU with 3.3 GHz and 8 GB installed memory.

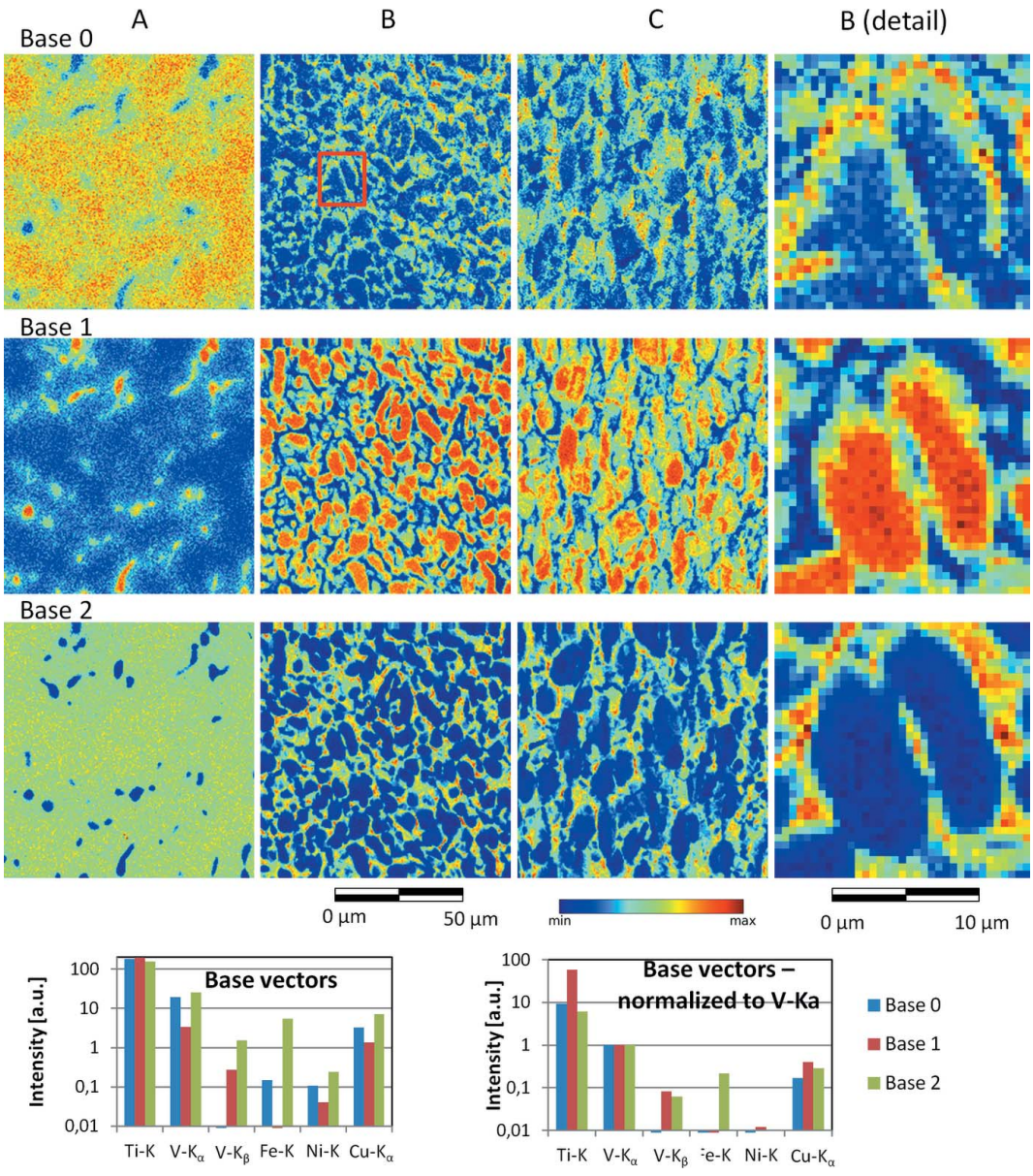

Figure 4
Bases obtained from a combined data set consisting of the elemental distribution images of the samples *A*, *B* and *C*. The coefficient images for the samples *A*, *B* and *C* are shown from left to right, with the detail of sample *B* (indicated in coefficient image of Base 1) shown in the rightmost column.

thickness until all the sample consists only of α phase rich in Ti and Al. Afterwards, the pure α phase is superimposed with a pure β layer until the sample is pure β phase again. The primary beam (11.5 keV) impinges on the sample at normal angle and the fluorescence radiation is detected in an angle of 5°. The model aimed at a qualitative reproduction of the effects, and not a quantitative reproduction of the measured data for a single sample with a specific concentration of trace elements in both phases and a specific detection angle.

XMIM-SIM was chosen for the simulation of these experiments, as it allows for fast MC without in depth programming knowledge and command line operations in a transparent, interactive fashion (Schoonjans *et al.*, 2012, 2013). Further, the software package provides a batch mode that allows for the variation of one or more parameters in a series of MC simulations without user-intervention.

In the upper part of Fig. 5 all signals are normalized to their maximum intensity and plotted against the thickness of the surface layer. In the middle part the signals were first normalized to the V-*KL*3 signal and then again normalized to fully exploit the value space between 0 and 1. The *KL*3 transitions are directly proportional to the element's K_α lines, while the *KM*3 transition corresponds to the K_β lines. In all elements but V, the absorption in the sample matrix is comparable for the K_α and K_β lines, so that they are not individually treated. In the case of V the K_α line (4.952 keV) is below the Ti-*K* edge (4.966 keV), while the K_β line (5.427 keV) is above it, therefore the V-K_β line is much stronger attenuated. This renders the line ratio of the V-*K* lines very sensitive to the structure of the sample.

It can be clearly seen that, in the case of superposition of any order, the signal of the stabilizing elements of the β phase

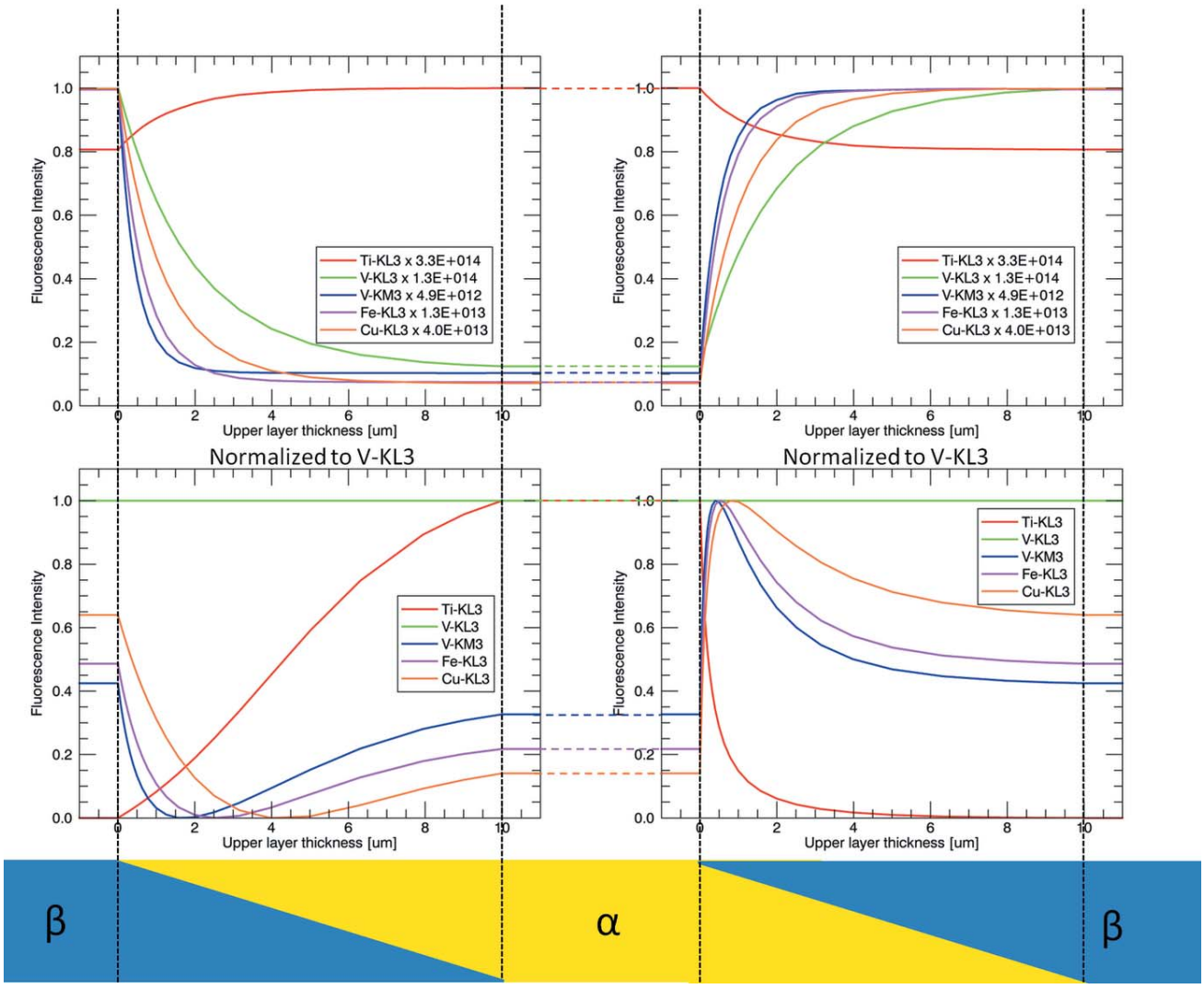

Figure 5
Results of the MC simulation using *XMIM-SIM*. On the left a superposition of the α phase (yellow) on the β phase (blue) is shown, and on the right the opposite is the case. In the two upper graphs the intensity of the given fluorescence line is normalized to its maximum value. In the two lower plots the intensity of all lines is shown relative to the V-*KL*3 and normalized to fully exploit the value space between 0 and 1. Dashed lines are to guide the eye only. The plots in one row of the figure use the same vertical axis.

(V, Fe and Cu) is enhanced relative to the composition of the pure α-phase and might be misinterpreted as an enrichment of these elements in the grain boundaries of primary α. However, normalizing all signals to the V-*KL*3 signal reveals an odd feature, which would not be observed in the case of enrichment: if the α phase is in superposition to the β phase the signals of all lines above the Ti-*K* edge (V-*KM*3, Fe-*KL*3 and Cu-*KL*3) are reduced (left part of Fig. 5). If the β is present above the α phase (right part of Fig. 5) an enhancement of these signals relative to the V-*KL*3 can be expected. Ni was not included in the model as it is a minor element not listed in the report of conformance of the as-received Ti-6Al-6V-2Sn alloy. However, its signal would be, if plotted, between that of Fe and Cu.

In the obtained data set four different components, *i.e.* phase combinations, should be present: α phase, β phase, α phase on β phase and β phase on α phase. While the phases in superposition do not represent clear components, but rather signal gradients, they can be approximated as such. However, NMF only reveals the presence of three bases: the Ti-rich primary α phase is represented by Base 1 (with minor contribution of Base 0), the V-rich β phase is represented by Base 2, and the overlap of α phase on β phase is highlighted in Base 0. Owing to the additive nature of NMF the missing case (β phase on α phase) is not represented as an individual base, but as a linear combination of the Bases 1 and 2. It can also be seen in Fig. 5 that this case is less pronounced than the superposition of α on β phase and signals similar to that of the bulk material are reached with only a few micrometres of β phase on the α phase.

MC allows confirmation of our assumption that absorption effects cause the elemental ratios giving rise to Base 0. In the upper and right interphases of the two primary α phase grains shown in detail in Figs. 2 to 4 the α phase is present at the

surface of the sample, above the β phase. This explains the anisotropic features visible in the coefficient images.

From the results of the virtual line scan shown in Fig. 5, elemental distribution images were calculated, reducing the intensity per pixel and adding statistical noise (see Fig. 6). The simulated image contains several α grains in a β matrix. To the left of each α grain the α phase is in superposition to the β phase, while to the right the opposite is the case. In the simulated data the gradient at the interphase is fully resolved, so the absorption effect on the ratio of V-K_β to V-K_α can be shown in the V-*KM*3/(V-*KM*3 + V-*KL*3) image. Here the presence of the β-phase on the surface results in a relative enhancement of the V-*KM*3 signal, while it is diminished in the case of the presence of the α-phase on the surface. This ratio image is much clearer than that in DSI 2.3 (see supporting information), given the better statistics per pixel.

The simulated data set was analyzed with NMF with identical parameters as the original data set, with the exception of the absence of the Ni signal. Typical results of these factorizations are shown in Fig. 6. Base 0 represents the superposition of the α on the β phase, Base 1 the α phase and Base 2 the β phase, which is identical to the results on the acquired real data sets and confirms our interpretation of the NMF results.

However, the NMF representation of the simulated data diverges from that of the measured data at two points. In the MC model the abundance of Fe in the α phase was overestimated, so that the Fe-*KL*3 load on Base 1 is also enhanced towards the measured data.

Further, probably due to this quantitative divergences between simulation and real data, Base 0 contributes not only to the area where the α-phase is present above the β phase but also to the pure β phase (strongly) and the pure α phase (weakly), as opposed to the real data, where Base 0 contributed to the pure α phase weakly and negligible to the β phase.

These quantitative differences notwithstanding, the factorization of the simulated data set has confirmed the interpretation of Base 0 as the result of superposition of phases in the sample.

3.4. Alternatives to the NMF approach used

Next to NMF other approaches to study the absorption effects were investigated. The most obvious alternative to NMF is PCA, which was also performed with the data set of sample *B* for comparison (shown in DSI 2.1 of the supporting information). Like NMF, it highlights the anisotropic phase represented by Base 0 in NMF, but it is less straightforward to be interpreted, as the representation obtained did not preserve the non-negative nature of elemental distribution images.

One can also directly investigate the ratio of two signals, either in the form of a scatter plot (V-K_α plotted against V-K_β) (shown in DSI 2.2 of the supporting information) or a ratio map [*e.g.* V-K_α/(V-K_α+V-K_β)] (shown in DSI 2.3 of the supporting information). This also provides some insight into absorption effects, but it requires a high degree of user intervention during data interpretation and is limited to the relation of two signals. In the case of the samples investigated, in the scatter plots of V-K_α against V-K_β, Fe and Cu, a broadening of elemental ratios was observed, but no sharp separation, as the statistics of the acquired data were insufficient for this.

Recently, Mak *et al.* described their non-negative matrix analysis tool included in the *MANTiS* software package for the analysis of spectromicroscopy data (Mak *et al.*, 2014). The basic NNMA (non-negative matrix approximation) algorithm was found to be comparable with the NMF one used

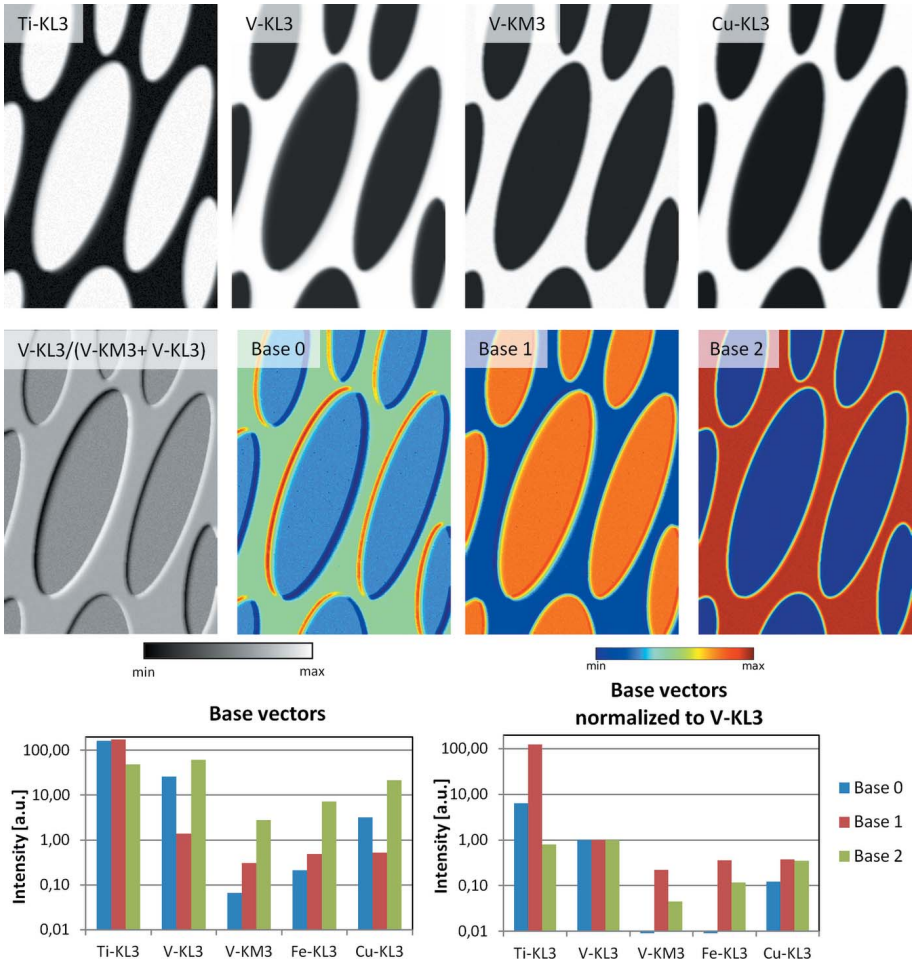

Figure 6
Artificial test data set, based on the results of the Monte Carlo simulation shown in Fig. 5 and its representation by NMF.

in this paper. However, they discussed alternatives to the Frobenius norm as quality criterion for NMF, mainly with respect to the analysis of full spectral data. One of their approaches was to cluster the sample after PCA and use the obtained cluster spectra as initial values for NMF. During NMF the similarity of the calculated basis vectors to the cluster spectra is used as a criterion of the quality of the factorization. We observed in our data set that this resulted in clearer representations with less variation and fewer 'failures'. However, we refrained from including a similar algorithm as it would require an interpretation of the PCA results and thus complicate the analysis. It also remains to be seen how far the bias of the data towards the cluster spectra does not also bias the representation away from minor components that might otherwise be found.

4. Conclusions

It has been shown that NMF is fast and provides easily interpretable representations unbiased by the user's expectations. It is also robust, as it can handle limited differences in sensitivity, *e.g.* due to variations in sample thickness and detection geometry.

This makes it a suitable tool for the correct near real-time analysis and interpretation of data acquired during XRF imaging experiments at synchrotron sources, as the emphasis of correlations and reduction of redundancies in the data sets supports the efficient use of the short experimental time allocated.

In the studied case, variations of the X-ray fluorescence intensity of several elements at the grain boundaries of primary α grains were studied for a bi-modal $\alpha+\beta$ Ti-6Al-6V-2Sn alloy. NMF analysis highlighted the anisotropic distribution of these variations in the samples *B* and *C*, which was not detected in sample *A*. This allowed, in combination with MC, to show that in sample *A* (heated to 940°C, ∼10 vol% of primary α grains dispersed in a β matrix) this effect is associated with concentration variations at the interphases of the bulk material, *i.e.* diffusion effects during the $\alpha \rightarrow \beta$ phase transformation. For microstructures formed by globular primary α grains (about 85 vol%) within a β matrix (samples *B* and *C*, heated to 530°C and 590°C, respectively), these signal intensity gradients are associated with the superposition of both phases.

Care needs to be taken when interpreting the representation in a quantitative way. Each representation is just one of many possible solutions and so the quantitative information in the basis vectors varies, typically by a few percent, between factorizations.

Beyond that, we could show that NMF is not limited to the interpretation of imaging data of single samples, but that it can be used to factorize data from several similar samples, yielding uniform basis vectors.

In general it can be said that NMF only provides minor insights in well known and well understood systems, but it tremendously supports the interpretation of less well understood ones. Furthermore, the easily understandable nature of base vectors and coefficients allows easily communicating correlations in complex data sets.

Acknowledgements

We thank T. Schoonjans (Bundesanstalt für Materialforschung und -prüfung, Berlin, Germany) for the support in using *XMIM-SIM*. The research leading to these results has received funding from the European Community's Seventh Framework Programme (FP7/2007-2013) under grant agreement No. 312284. The German Federal Ministry of Education and Research (BMBF) is acknowledged for the financial support (Verbundprojekt 05K2012). GR and PBV would like to acknowledge the K-Project 'Non-destructive testing and tomography Plus' supported by the COMET-Program of the Austrian Research Promotion Agency (FFG) and the provinces of Upper Austria (LOÖ) and Styria (STMK).

References

Alfeld, M. & Janssens, K. (2015). *J. Anal. At. Spectrom.* **30**, 777–789.
Alfeld, M., Wahabzada, M., Bauckhage, C., Kersting, K., Wellenreuther, G. & Falkenberg, G. (2014). *J. Phys. Conf. Ser.* **499**, 012013.
Banerjee, D. & Williams, J. C. (2013). *Acta Mater.* **61**, 844–879.
Barriobero-Vila, P., Requena, G., Buslaps, T., Alfeld, M. & Boesenberg, U. (2015*a*). *J. Alloys Compd.* **626**, 330–339.
Barriobero-Vila, P., Requena, G., Warchomicka, F., Stark, A., Schell, N. & Buslaps, T. (2015*b*). *J. Mater. Sci.* **50**, 1412–1426.
Boesenberg, U., Falk, M., Ryan, C. G., Kirkham, R., Menzel, M., Janek, J., Fröba, M., Falkenberg, G. & Fittschen, U. E. A. (2015). *Chem. Mater.* **27**, 2525–2531.
de Juan, A., Tauler, R., Dyson, R., Marcolli, C., Rault, M. & Maeder, M. (2004). *TrAC Trends Anal. Chem.* **23**, 70–79.
Kéri, A., Osán, J., Fábián, M., Dähn, R. & Török, S. (2016). *X-ray Spectrom.* **45**, 54–62.
Kotula, P. G., Keenan, M. R. & Michael, J. R. (2003). *Microsc. Microanal.* **9**, 1–17.
Lahlil, S., Cotte, M., Biron, I., Szlachetko, J., Menguy, N. & Susini, J. (2011). *J. Anal. At. Spectrom.* **26**, 1040.
Lee, D. D. & Seung, H. S. (1999). *Nature (London)*, **401**, 788–791.
Mak, R., Lerotic, M., Fleckenstein, H., Vogt, S., Wild, S. M., Leyffer, S., Sheynkin, Y. & Jacobsen, C. (2014). *Faraday Discuss.* **171**, 357–371.
Mishra, S., Wellenreuther, G., Mattusch, J., Stärk, H.-J. & Küpper, H. (2013). *Plant Physiol.* **163**, 1396–1408.
Monico, L., Janssens, K., Alfeld, M., Cotte, M., Vanmeert, F., Ryan, C. G., Falkenberg, G., Howard, D. L., Brunetti, B. G. & Miliani, C. (2015). *J. Anal. At. Spectrom.* **30**, 613–626.
Osán, J., Kéri, A., Breitner, D., Fábián, M., Dähn, R., Simon, R. & Török, S. (2014). *Spectrochim. Acta B*, **91**, 12–23.
Ryan, C. G. & Jamieson, D. N. (1993). *Nucl. Instrum. Methods Phys. Res. B*, **77**, 203–214.
Santos, H. C., Caliri, C., Pappalardo, L., Catalano, R., Orlando, A., Rizzo, F. & Romano, F. P. (2016). *Microchem. J.* **124**, 241–246.
Schoonjans, T., Solé, V. A., Vincze, L., Sanchez del Rio, M., Appel, K. & Ferrero, C. (2013). *Spectrochim. Acta B*, **91**, **82**, 36–41.

Schoonjans, T., Vincze, L., Solé, V. A., Sanchez del Rio, M., Brondeel, P., Silversmit, G., Appel, K. & Ferrero, C. (2012). *Spectrochim. Acta B*, **91**, **70**, 10–23.
Schroer, C. G., Boye, P., Feldkamp, J. M., Patommel, J., Samberg, D., Schropp, A., Schwab, A., Stephan, S., Falkenberg, G., Wellenreuther, G. & Reimers, N. (2010). *Nucl. Instrum. Methods Phys. Res. A*, **616**, 93–97.
Solé, V. A., Papillon, E., Cotte, M., Walter, P. & Susini, J. (2007). *Spectrochim. Acta B*, **91**, **62**, 63–68.
Vekemans, B., Janssens, K., Vincze, L., Adams, F. & Van Espen, P. (1994). *X-ray Spectrom.* **23**, 278–285.
Vekemans, B., Janssens, K., Vincze, L., Aerts, A., Adams, F. & Hertogen, J. (1997). *X-ray Spectrom.* **26**, 333–346.
Vogt, S. (2003). *J. Phys. IV*, **104**, 635–638.